ADVANCED MATERIALS
www.advmat.de

Unraveling the Capacitive Behaviors in Nanoconfined Ionophilic Carbon Pores

Xinyuan Li, Congcong Cai, Liang Zhou, Liqiang Mai,* and Hong Jin Fan**

Intensifying the synergy between confined carbon nanopores and ionic liquids (ILs) and a deep comprehension of the ion behavior is required for enhancing the capacitive storage performance. Despite many theoretical insights on the storage mechanism, experimental verification has remained lacking due to the intricate nature of pore texture. Here, a compressed micropore-rich carbon framework (CMCF) with tailored monolayer and bilayer confinement pores is synthesized, which exhibits a compatible ionophilic interface to accommodate the IL [EMIM][BF_4]. By deploying in situ Raman spectroscopy, in situ Fourier-transform infrared spectroscopy, and solid-state nuclear magnetic resonance, the effect of the pore textures on ions storage behaviors is elucidated. A voltage-induced ion gradient filling process in these ionophilic pores is proposed, in which ion exchange and co-ion desorption dominate the charge storage process. Moreover, it is established that the monolayer confinement of ions enhances the capacity, and bilayer confinement facilitates the charging dynamics. This work may guide the design of nanoconfinement carbon for high-energy-density supercapacitors and deepen the understanding of the charge storage mechanism in ionophilic pores.

1. Introduction

Among electrochemical energy storage systems, supercapacitors possess the advantages of high power density and long lifespan, owing to the electrostatic separation of ions at the electrode/electrolyte interface without involving sluggish Faradic reactions.[1] In the pursuit of high energy density, extensive endeavors have been dedicated to understanding the capacitive behavior of ion confinement in nanoporous carbon.[2] A favored carbon electrode material should have the merits of a large specific surface area, rapid ion delivery, and high electrical conductivity.[3] Ionic liquids (ILs), composed of solely cations and anions, are esteemed for their electrochemical stability and ability to offer a wide voltage window, rendering them a preferred electrolyte option for capacitive energy storage.[4] While maximum capacitance and energy density are achievable when the pore size aligns with that of ILs, this comes at the expense of compromised charging dynamics.[5] Hence, striking a balance between energy density and charging dynamics of carbon electrode materials entails judicious engineering of the pore texture.

The capacitance performance is governed by the electrochemical double layer structure at the electrode/electrolyte interfaces.[6] In this work, a widely used IL, [EMIM][BF_4], is employed as electrolyte to match ionophilic carbon pores. The sizes of 1-ethyl-3-methylimidazolium ($[EMIM]^+$) and tetrafluoroborate ($[BF_4]^-$) are depicted in **Scheme 1**.[7] The ion bilayer demonstrates minimum and maximum sizes of 0.88 and 1.33 nm, respectively. Pores larger than $[EMIM]^+$ (0.76 nm) are beneficial for its adsorption. In ILs, the absence of a solvation shell gives rise to strong electrostatic Coulombic forces between adjacent ions, resulting in Coulombic ordering of each ion surrounded by oppositely charged ions.[8] Pores greater than 1.33 nm indicate non-confinement with Coulombic ordering (Scheme 1a). Within the range of pores from 0.88 to 1.33 nm, ions are in bilayer confinement with Coulombic ordering (Scheme 1b). When the pore size falls between 0.76 and 0.88 nm, strong interactions between the carbon wall and ions generate image charges, leading to a reduction in interionic interactions and the disruption of Coulombic ordering (Scheme 1c).[8b,9] Consequently, ions are confined within monolayer pores, forming superionic states with ion pairs. Upon negatively charging the electrode, the over-screening effect, resulting in double-layer loss, takes place at pores larger than 1.33 nm (Scheme 1d).[10] Here, an excess of $[EMIM]^+$ accumulates at the surface, while the surplus positive charge is neutralized by $[BF_4]^-$ ions in the sublayer. Pores with bilayer confinement prevent the over-screening effect and induce the monolayer arrangement of $[EMIM]^+$ perpendicular to the wall, thereby enhancing charge

X. Li, C. Cai, L. Zhou, L. Mai
State Key Laboratory of Advanced Technology for Materials Synthesis and Processing
Wuhan University of Technology
Wuhan 430070, P. R. China
E-mail: liangzhou@whut.edu.cn; mlq518@whut.edu.cn
X. Li, H. J. Fan
School of Physical and Mathematical Sciences
Nanyang Technological University
Singapore 637371, Singapore
E-mail: fanhj@ntu.edu.sg
L. Zhou, L. Mai
Hubei Longzhong Laboratory
Wuhan University of Technology (Xiangyang Demonstration Zone)
Xiangyang, Hubei 441000, P. R. China

The ORCID identification number(s) for the author(s) of this article can be found under https://doi.org/10.1002/adma.202404393

DOI: 10.1002/adma.202404393

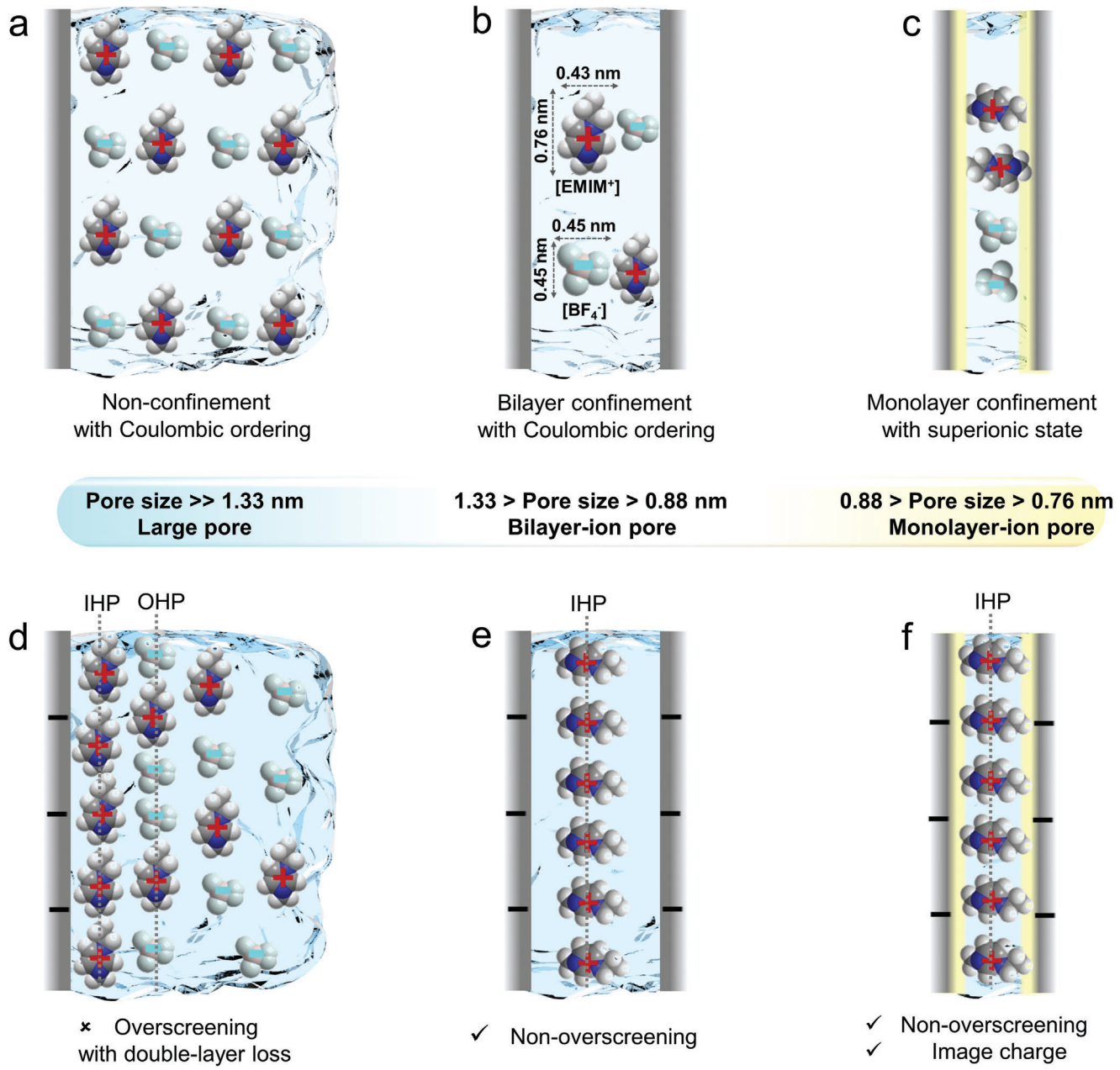

Scheme 1. Sorption behaviors of [EMIM][BF_4] in ionophilic carbon pores. Schematics of [EMIM][BF_4] residing in pores with sizes: a) greater than 1.33 nm (large pore), b) between 0.88 and 1.33 nm (bilayer-ion pore), and c) between 0.76 and 0.88 nm (monolayer-ion pore) in the absence of an applied potential. d–f) The corresponding electrode/electrolyte interfaces upon negative charging.

storage and facilitating ion diffusion (Scheme 1e). The lateral arrangement of $[EMIM]^+$ in negatively charged bilayer-ion pores could be the optimal configuration for high storage density and rapid dynamics. Crucially, pores with monolayer confinement will also circumvent the over-screening effect, whereas the strong interactions between the carbon wall and ions contribute to enhanced capacitance (Scheme 1f). The absence of over-screening in both bilayer and monolayer confinement pores guarantee the efficient charge storage. At present, the understanding of ion storage mechanisms in nanoporous confined spaces has been predominantly provided by isolated theoretical calculations,[11] while experimental direct evidence is scanty which poses a challenge in reliable materials science and in situ characterization techniques.

This study endeavors to engineer carbon to enhance energy density and charging dynamics and also unravel the capacitive behaviors in ionophilic pores. We synthesized the compressed micropore-rich carbon framework (CMCF) via hydrogen bond (H-bond) induced compression followed by KOH activation. This carbon structure contains monolayer and bilayer confinement pores, along with an ionophilic interface, rendering CMCF with high capacitance and rate performance as well as energy density. Solid-state nuclear magnetic resonance (ssNMR) reveals subtle

confinement in the coupled monolayer and bilayer confinement pores, facilitating ion dynamics. In situ Raman spectroscopy dynamically identifies variations in the interaction between the carbon wall and $[EMIM]^+$ with varying voltages. In situ Fourier-transform infrared (FTIR) spectroscopy unveils the ion exchange and co-ion desorption mechanisms. Theoretical calculations reveal the role of bilayer confinement pores in governing charging kinetics, the importance of monolayer confinement pores in enhancing capacitance storage, as well as the challenges posed by excessively small pores during the entry process. This study provides insights into ion behaviors within ionophilic confinement carbon pores and their effects on capacitive energy storage performance.

2. Results and Discussion

The construction of CMCF is schematically illustrated in **Figure** 1a. Initially, carbon nanotube@3-aminophenol-formaldehyde resin (CNT@APF) nanofibers are synthesized by the polymerization of 3-aminophenol and formaldehyde on CNTs in aqueous solution.[5c,12] The strong H-bond interactions between amino and hydroxyl groups, as detected by FTIR spectroscopy (Figure S1a, Supporting Information), transform the loose CNT@APF nanofibers into compressed carbon framework (CCF) during carbonization. The activation process enlarges the sizes and increases the number of the monolayer and bilayer confinement pores for CMCF. The CNT core serves as both a conductive and mechanical skeleton, promoting electron transport and facilitating ion mobility by preventing excessive compression of the 3D nanofiber framework (Figure 1b). The pore sizes of CMCF exceed those of $[EMIM]^+$ and $[BF_4]^-$, indicating full accessibility of the active surface to the electrolyte ions. The CNTs have a diameter of ≈10 nm and lengths up to several micrometers. The core–shell structured CNT@APF nanofibers with a diameter of ≈60 nm are loosely cross-linked (Figure 1c; Figure S2a,b, Supporting Information). High-angle annular dark-field scanning transmission electron microscopy (HAADF-STEM) images and the corresponding energy-dispersive X-ray spectroscopy (EDS) elemental mappings manifest the homogeneous distribution of C, N, and O (Figure S3a, Supporting Information). The CCF displays tight cross-linking with a slight reduction in diameter to ≈50 nm (Figure 1d, Figure S2c,d, Supporting Information), demonstrating good thermal stability as verified by thermal gravimetric analysis (TGA) (Figure S1b, Supporting Information). The CMCF features fine-tuned micropores and negligible size reduction compared to CCF (Figure 1e, Figure S2e,f, Supporting Information), indicating heightened corrosion resistance. The H-bond compression strategy endows nanofibers with tap densities (0.22 g cm^{-3}) comparable to microspheres (0.24 g cm^{-3}) (as seen in digital photos 5 and 6, Figure 1f). Dynamic contact angle measurements demonstrate the well wettability of CMCF toward $[EMIM][BF_4]$, with an initial value of 39.6° and ≈0° after 4 min (Figure 1g).

Without the introduction of CNTs, solid APF microspheres are obtained with a diameter of 600 nm. After carbonization, the diameter decreases to 500 nm, which further reduces to 470 nm for the final product of micropore-rich carbon spheres (MCS) (Figure S4, Supporting Information). Yield measurement indicates that CNTs enhance polymerization efficiency by 23% and confer higher thermal resistance, resulting in a 43.1% increase in yield (Figure S5 and Table S1, Supporting Information). X-ray diffraction (XRD) patterns of all the samples (CMCF, CCF, and MCS) show broad peaks at ≈23° and 43°, indicative of amorphous carbon (Figure S6a, Supporting Information).[13] These diffraction peaks weaken in CMCF and MCS due to an increased number of defects after activation, which will benefit ion accommodation. Raman spectra exhibit a typical D-band at ≈1340 cm^{-1} and a G-band at ≈1590 cm^{-1} (Figure S6b, Supporting Information). The I_D/I_G ratio of MCS is 0.98, suggesting the amorphous features.[14] The CMCF and CCF exhibit a 2D-band ≈2700 cm^{-1} and a heightened G-band associated with the CNT core relative to MCS.

The electrochemical behaviors at the electrode/electrolyte interface are intricately associated with the pore texture, confinement degree, and surface chemistry of carbon materials. N_2 adsorption/desorption isotherms present a sharp increase at $P/P_0 < 0.1$ and hysteresis at $P/P_0 > 0.8$, indicating abundant micropores with certain number of mesopores (**Figure** 2a).[15] Owing to its abundant micropores and meso-/macropores in the fibrous framework, the CMCF displays a higher specific surface area and pore volume (2405 m^2 g^{-1}, 2.22 cm^3 g^{-1}) than the CCF (362 m^2 g^{-1}, 0.55 cm^3 g^{-1}) and MCS (770 m^2 g^{-1}, 0.39 cm^3 g^{-1}). Pore size distribution reveals two peaks at 0.78 and 1.32 nm in CMCF (Figure 2b; Figure S7, Supporting Information), corresponding to monolayer and bilayer confinement pores for $[EMIM]^+$ (0.76 nm) and $[BF_4]^-$ (0.45 nm). For neat $[EMIM][BF_4]$, the ^1H NMR presents five chemical environments for ^1H peaks (Figure 2c). The additional peak at 4.7 ppm comes from the solvent (D_2O). For the CMCF soaked with $[EMIM][BF_4]$, ssNMR exhibits a broad ^1H peaks assigned to ex-pore $[EMIM]^+$. Such a situation corresponds to the local magnetic field effect stemming from the circulating delocalized π electrons of surrounding carbon walls. The *2 and *3 peaks with similar chemical shifts merge into a single broad peak due to the restricted molecular motion in ssNMR. Compared to neat $[EMIM][BF_4]$, the signals of ex-pore $[EMIM]^+$ for CMCF soaked with $[EMIM][BF_4]$ shift to a lower frequency by 0.5 ppm. In-pore resonance of $[EMIM]^+$ inside the micropores adjacent to carbon surfaces is also detected. The slight split peak at −0.1 ppm ascribed to in-pore $[EMIM]^+$ suggests weak confinement of carbon pores, which will benefit the charging dynamics.[16] X-ray photoelectron spectroscopy (XPS) measurement (Figure S8, Supporting Information) reveals that the CMCF, after secondary carbonization in a reduction atmosphere, showcases higher levels of stable pyridinic-N and fewer heterogeneous atoms compared to CCF and MCS. The high pyridinic-N content in CMCF results from its higher pore density.[17]

There are scarce reports on the electrochemical behaviors of ionophilic nanoporous carbon owing to its intricate nature, not to mention real-time monitoring of capacitive behavior in ionophilic pores. In situ Raman analysis of carbon electrodes has been primarily employed in battery research to detect the change in carbon structure resulting from Faradaic reactions.[18] However, detecting changes in carbon structure in supercapacitors is challenging as the change is much less pronounced due to the physical adsorption/desorption processes. In this study, the strong Coulomb forces inherent in ILs and the interaction between ions and nanoconfined carbon walls resemble the ion

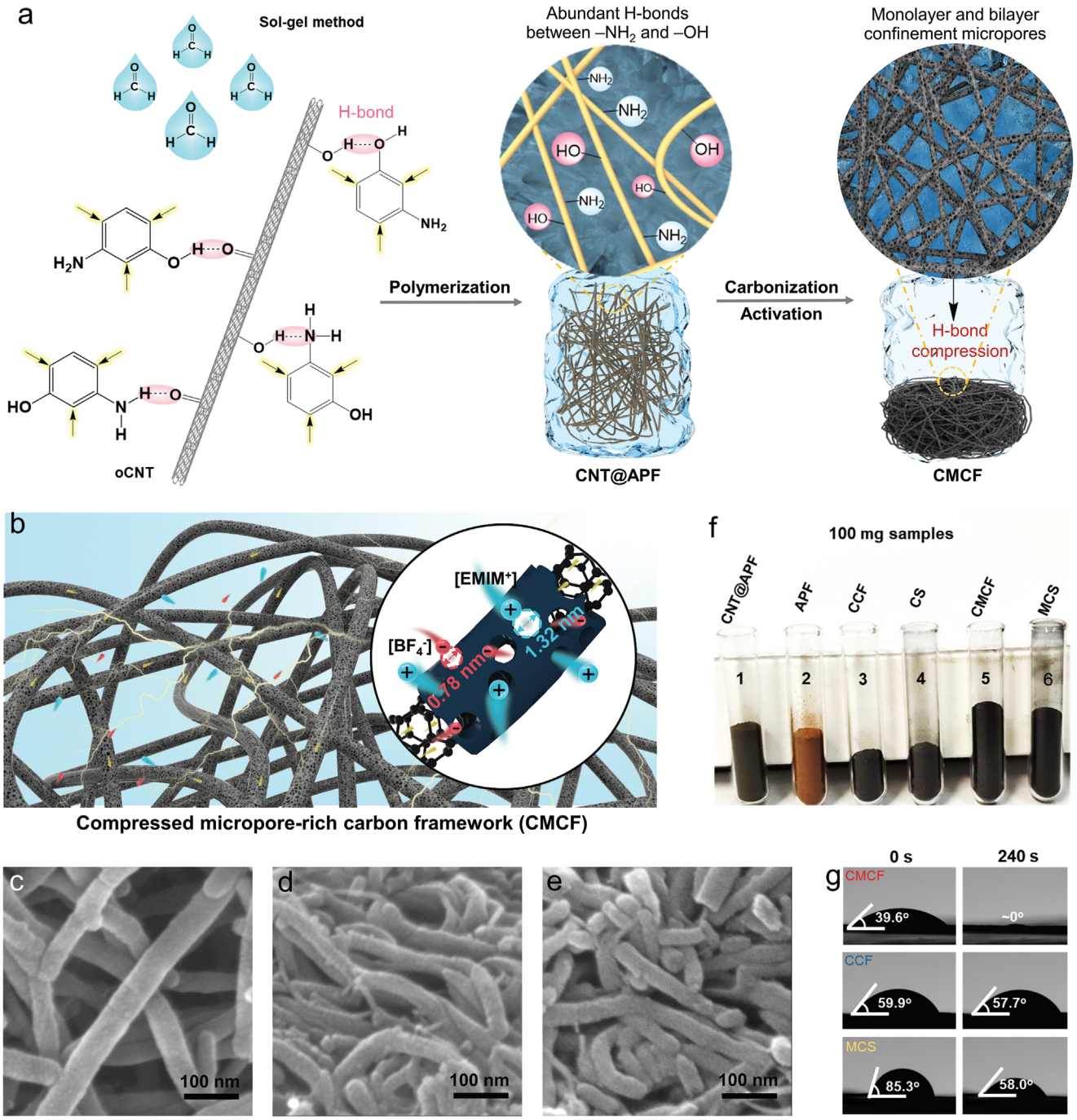

Figure 1. Formation of carbon fibers with ionophilic nanoconfinement pores. a) Construction of CMCF driven by H-bonds with subsequent carbonization and activation. b) Depiction of [EMIM][BF_4] storage in monolayer and bilayer confinement ionophilic pores of CMCF. SEM images of c) CNT@APF, d) CCF, and e) CMCF. f) Digital photos showing volume comparisons for each 100 mg sample. 1, 3, and 5 are fiber-shaped particles. 2, 4, and 6 are sphere-shaped particles. g) Dynamic contact angles at initial and after 4 min stages for [EMIM][BF_4].

intercalation reactions. This inspires us to conduct the in situ Raman characterization of capacitive behavior in ionophilic confined carbon pores. Pores in carbon materials can be categorized into three types based on accessibility: through pores, blind pores, and closed pores (Figure 2d).[19] The through pores allow surface access and ion transport via interconnected channels, while the blind pores are accessible but unable to transport ions due to narrow entrances and closed exits. Closed pores are inaccessible with sealed walls.

To reveal the ion behaviors at CMCF/[EMIM][BF_4] interface, in situ Raman analysis was performed on the CMCF negative electrode (Figure S9, Supporting Information). The

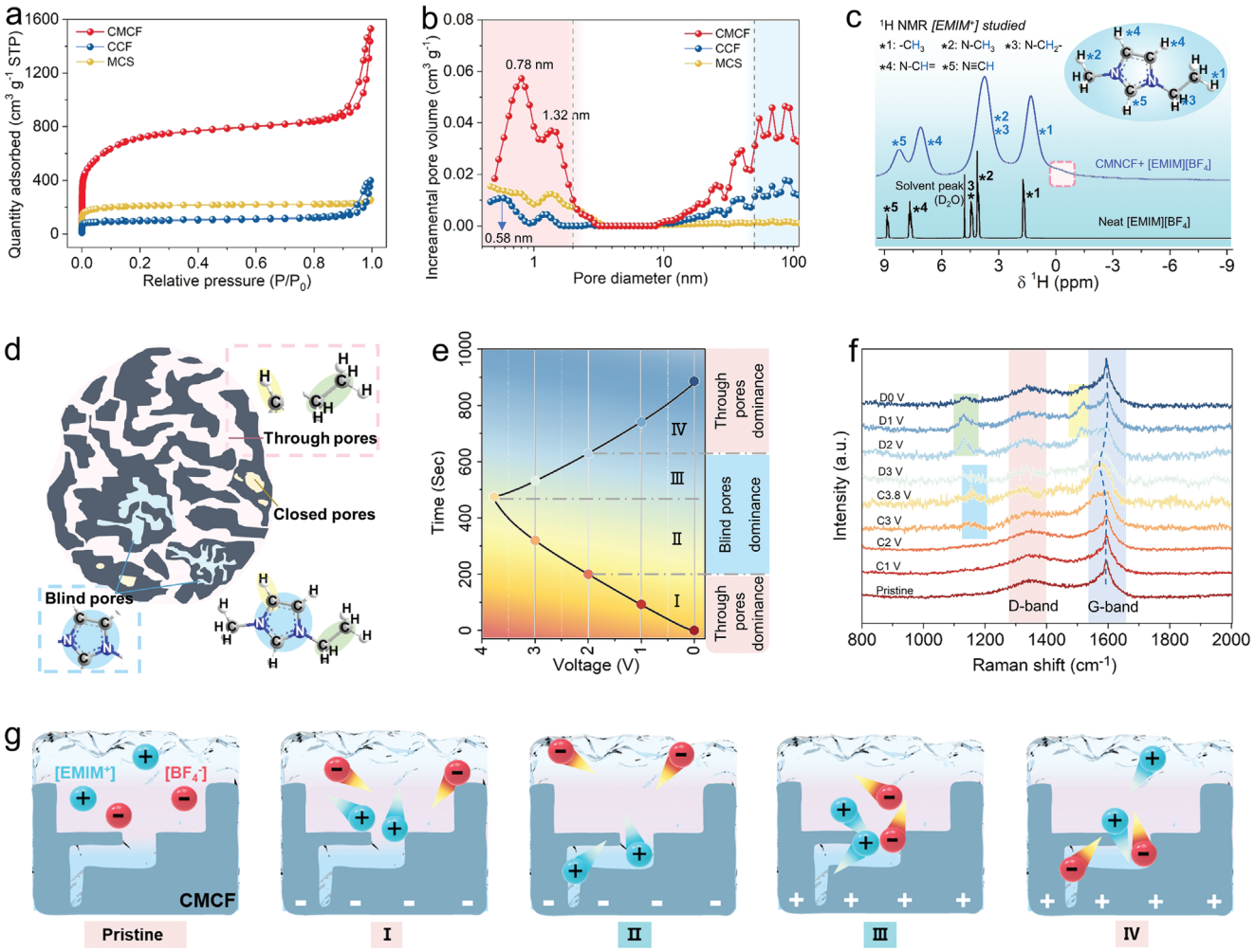

Figure 2. Characterization of ion behaviors at CMCF/[EMIM][BF_4] interface. a) N_2 adsorption/desorption isotherms. The inset is the SEM image of MCS. b) Corresponding pore size distributions. c) ^{1}H NMR spectra of CMCF+[EMIM][BF_4] mixture and neat [EMIM][BF_4]. d) Diagram illustrating the typical three types of pores in porous carbon materials. e) GCD curve of CMCF electrode at 1 A g^{-1}. f) In situ Raman spectra. g) Schematic illustration of the voltage-induced ion gradient filling in blind pores and through pores.

electrochemical processes can be classified into four stages (Figure 2e). Two changes are notable: one is the shift and broadening of the G band; the other is the vibrations associated with $[EMIM]^+$ (Figure 2f). At state I (0–2 V), the capacitance primarily arises from $[EMIM]^+$ absorption and $[BF_4]^-$ desorption in through pores, with minimal change observed in the position and shape of the G-band (Figure 2g). At state II (2–3.8 V), the charge storage predominantly occurs in blind pores, as indicated by the redshift of the G-band. The migration of $[EMIM]^+$ from through pores into blind pores can be inferred from the strong ring in-plane asymmetric vibration of $[EMIM]^+$ at 1154 cm^{-1}, associated with the squeezing by narrow carbon pores. At high voltages, the strong Coulombic forces between $[EMIM]^+$ and $[BF_4]^-$ are weakened and cations will more readily enter the blind pores. When $[EMIM]^+$ distorts into the blind pores, strong interactions between $[EMIM]^+$ and carbon walls lead to the broadening and shifting of the G-band. At state III (3.8–2.0 V), as $[EMIM]^+$ migrates back from blind pores to through pores and exits the through pores, the G-band blueshifts to its initial position. At state IV (2.0–0 V), the exit of $[EMIM]^+$ from confinement pores leads to intense C–C stretching vibration at 1131 cm^{-1} and C–H asymmetric bending vibration at 1513 cm^{-1}. As the concentration of $[EMIM]^+$ within the confinement pores decreases, these vibration signals attenuate.[20] Based on this discussion, we propose a concept of voltage-induced ion gradient filling effect in nanopores, wherein capacitance contributions above 2 V predominantly arise from blind pores, while those below 2 V primarily stem from through pores.

To monitor the ingress and egress of $[EMIM]^+$ and $[BF_4]^-$ in the pores, in situ attenuated total reflection-FTIR (ATR-FTIR) was employed on the CMCF negative electrode. The in situ infrared cell comprises symmetric CMCF electrodes separated by a cellulose membrane soaked with [EMIM][BF_4] (**Figure 3a**). The infrared source is incident at a 45° angle onto the ZnSe optical crystal to detect $[EMIM]^+$ (1172 cm^{-1}) and $[BF_4]^-$ (1050 cm^{-1}) signals on the carbon electrode surface, resulting in signal attenuation upon ion entry into the carbon pores and enhancement upon ion exit.[21] During the charging process, the absorption

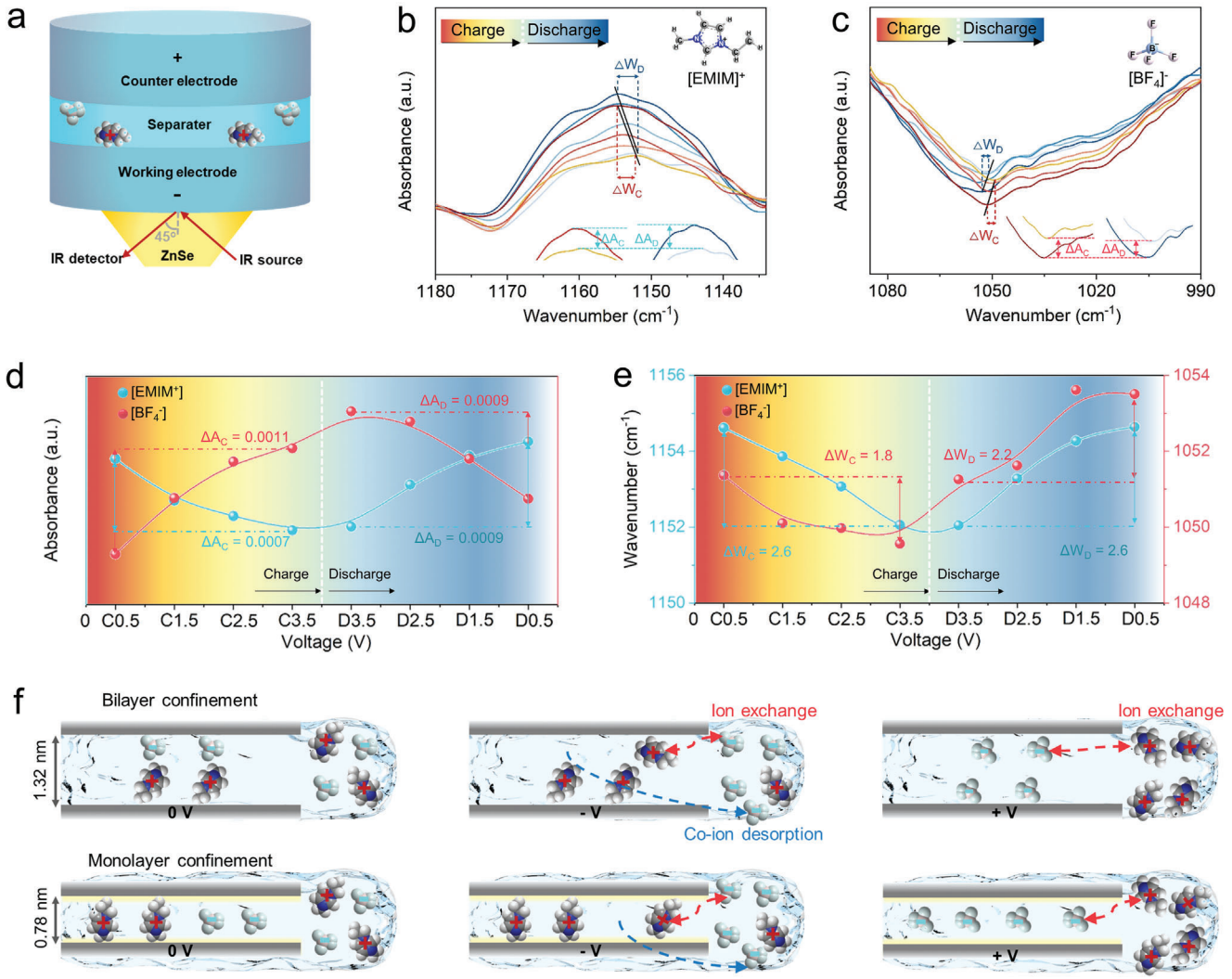

Figure 3. Charge-storage mechanism for CMCF in [EMIM][BF_4]. a) Schematic illustration of the in situ ATR-FTIR electrochemical test in this study. In situ ATR-FTIR spectra of b) $[EMIM]^+$ and c) $[BF_4]^-$. Insets are locally amplified spectra. d) Absorbance variation of the $[EMIM]^+$ and $[BF_4]^-$ peaks at different charge–discharge states, and e) corresponding wavenumber shift. f) Schematic illustration of the charge-storage mechanism in bilayer confinement and monolayer confinement pores in the unbiased, negatively, and positively biased states.

of $[EMIM]^+$ within the carbon pore leads to a reduction in absorbance (Figure 3b), while the simultaneous expulsion of $[BF_4]^-$ corresponds to enhanced absorbance (Figure 3c). The above change of absorbance reverses during the discharging process. Upon the initial charge process (Figure 3d), the lower influx of $[EMIM]^+$ into the pores compared to efflux in CMCF indicates the ion exchange and co-ion desorption mechanism.[22] During discharging, the $[EMIM]^+$ efflux is comparable to $[BF_4]^-$ influx, demonstrating the dominant ion exchange mechanism. Both $[EMIM]^+$ and $[BF_4]^-$ peaks undergo a redshift during charging due to ion interaction with confined carbon walls (Figure 3e) and image charges generated.[23] This peak shift is reversed during discharge. The $[EMIM]^+$ peak redshift in a greater degree compared to that of $[BF_4]^-$ owing to its better size compatibility with carbon pores.

Based on the above discussions, the charge storage mechanism in ionophilic CMCF is illustrated in Figure 3f.[24] In bilayer confinement pores, ions exhibit Coulomb ordering, while in monolayer confinement pores, ions exist in a superionic state as ion pairs. Both scenarios involve ion exchange and co-ion desorption upon charging. Negative-biased bilayer confinement pores yield monolayer $[EMIM]^+$ arrangements, while positive-biased ones yield a mixture of monolayer and bilayer $[BF_4]^-$ arrangements. As for the monolayer confinement pores, monolayer arrangements of $[EMIM]^+$ and $[BF_4]^-$ occur under negative and positive bias, respectively.[25]

Symmetrical supercapacitors are assembled to evaluate the capacitive storage capability of CMCF by employing [EMIM][BF_4] as the electrolyte (**Figure 4a**). To determine the optimal voltage window, cyclic voltammetry (CV) and galvanostatic charge–discharge (GCD) tests were employed, and the voltage window of the two-electrode coin-cell was varied from 2.0 to 4.0 V.[26] CV curves ranging from 2.0 to 3.8 V display obvious rectangular shapes (Figure 4b), while the corresponding GCD curves

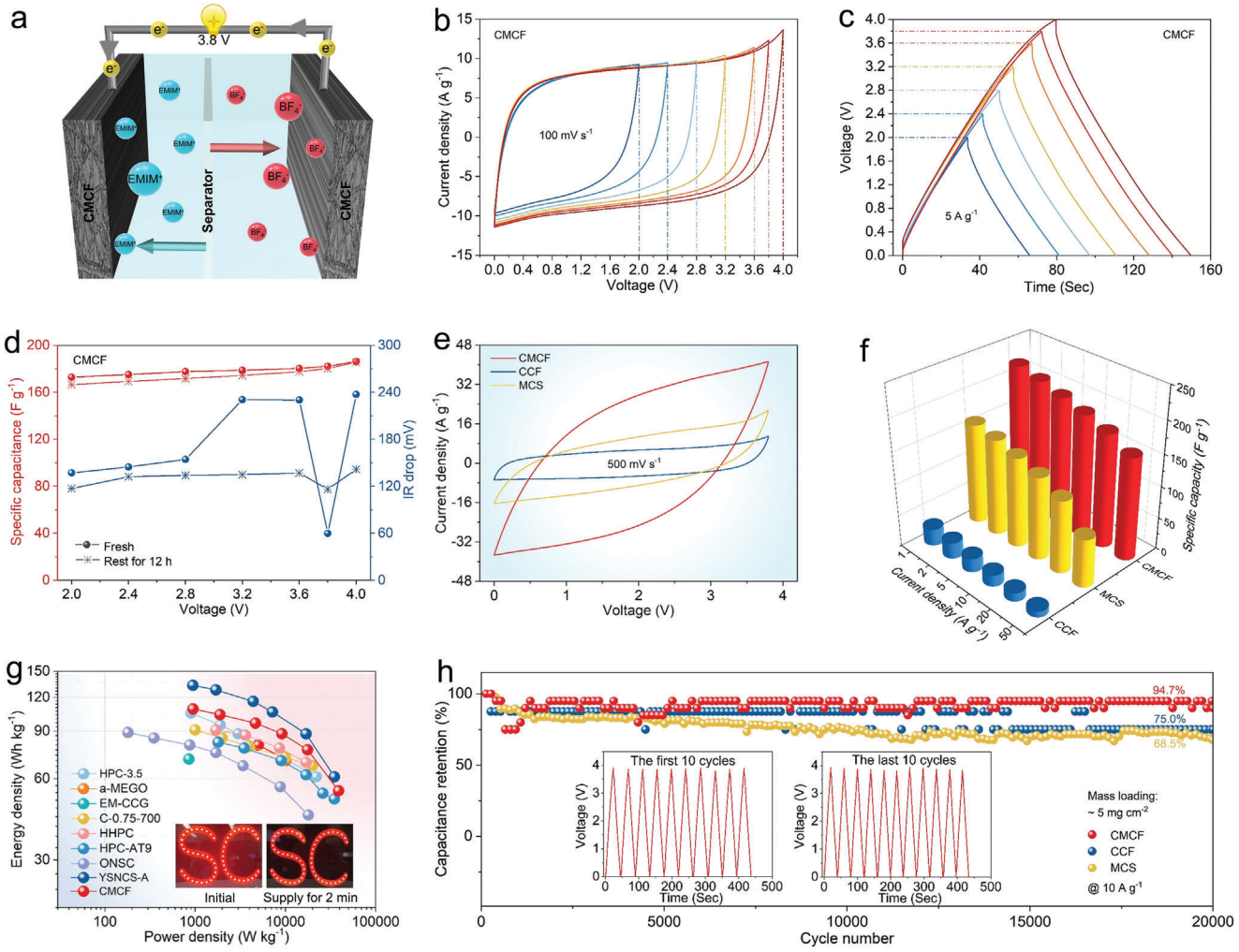

Figure 4. Electrochemical performance of supercapacitor in [EMIM][BF_4] IL electrolyte. a) Schematics illustration of the symmetrical supercapacitor device. b) Representative CV profiles at 100 mV s^{-1} and c) GCD curves at 5 A g^{-1} for CMCF at various operation voltages. d) Evolution of specific capacitance and IR drop of symmetrical devices from the fresh state and resting state for 12 h. e) CV profiles comparison at 500 mV s^{-1}. f) Specific capacitance comparison at various current densities. g) Comparison of energy and power densities of CMCF with other carbonaceous materials in IL electrolytes.[6a,12,27] The insets show 52 red LEDs being powered by a single device. h) Stability comparison of the three electrodes at 10 A g^{-1} for 20 000 cycles in [EMIM][BF_4] ILs. Insets are the GCD curves of the first and last ten cycles of CMCF.

exhibit almost symmetrical triangular shapes (Figure 4c), indicating characteristic capacitive performance and high reversibility. The sharpening of CV and the flattening of GCD at 4.0 V suggest the occurrence of redox reactions, which is harmful to electrochemical stability. The specific capacitance shows an increase with the applied voltage windows, potentially attributed to the image charge caused by ion twisting as ions squeeze through the blind pores at elevated voltages. As voltage rises, ions crowding in the pores cause an increased IR drop (Figure 4d). Low voltages impede ion entry into blind pores, resulting in a high IR drop, whereas excessively high voltages deteriorate the stability of the electrode/electrolyte interface, leading to another high IR drop. The minimal IR drop observed at 3.8 V indicates optimal ion dynamics and interfacial stability in the confinement pores.[26b] After resting for 12 h, the change in IR drop illustrates that the full IL wetting promotes the formation of a stable interface. Simultaneously, a slight decrease in capacitance is observed owing to deep infiltration of ions into the pores which reduces the net ion flow.

Based on the above results, all samples were evaluated within the voltage range of 0–3.8 V. Compared to CCF and MCS, the CMCF demonstrates a higher response current density, indicating its better capacitive performance (Figure 4e). With the increase in scan rate, the CV shape changes from rectangular to spindle shape (Figure S10, Supporting Information). At a mass loading of 2.7 mg cm^{-2}, the CMCF delivers a capacitance of 218 F g^{-1} at 1 A g^{-1}, surpassing CCF (26 F g^{-1} at 1 A g^{-1}) and MCS (157 F g^{-1} at 1 A g^{-1}) (Figure S11, Supporting Information). The GCD curves of CMCF at 1–50 A g^{-1} reveal the good rate performance (160 F g^{-1} at 50 A g^{-1} with 73.3% retention at 1 A g^{-1}) and negligible IR drop, which can be ascribed to the multiple beneficial factors, including slight confinement in monolayer and bilayer pores, continuous electron and ion transfer paths, and a 3D carbon framework (Figure 4f; Figure S12, Supporting

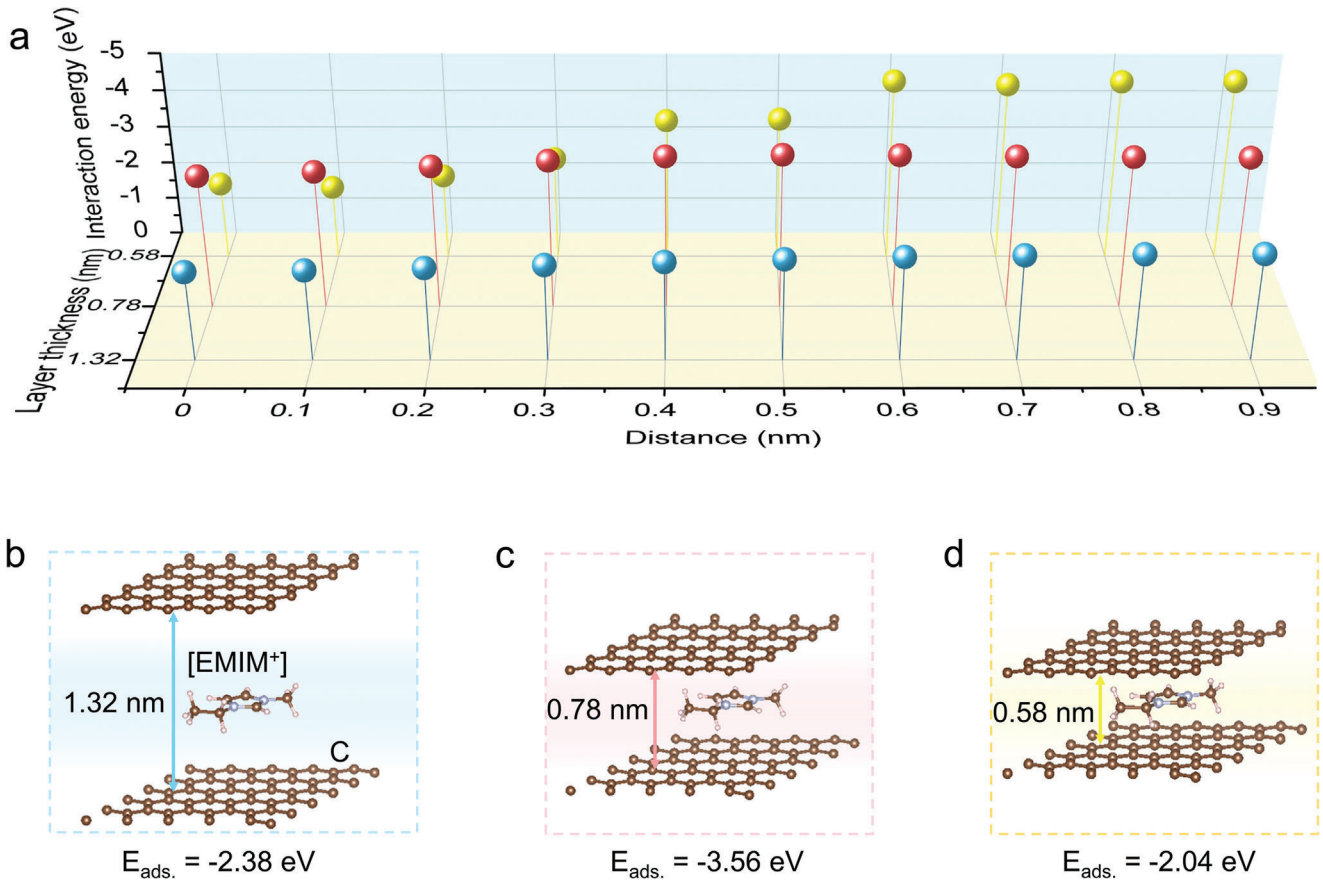

Figure 5. DFT simulations of [EMIM$^+$] diffusion in nanopores. a) Interaction energies of [EMIM$^+$] as a function of distance from the center of pores. Optimized structures of [EMIM$^+$] adsorbed on double-layer graphene with layer distances of b) 1.32 nm, c) 0.78 nm, and d) 0.58 nm.

Information). Ragone plots (Figure 4g) demonstrate that the symmetric supercapacitor device exhibits a high energy density of 108.8 Wh kg^{-1} at 946.3 W kg^{-1} and 54.2 Wh kg^{-1} at 39 000 W kg^{-1} (based on the active mass of CMCF), surpassing most porous carbons in ILs electrolytes.[6a,12,27] A single coin cell can illuminate an array of 52 light-emitting diodes (LEDs) for more than 2 min. The CMCF exhibits a capacitance retention of 94.7% at 10 A g^{-1} for 20 000 cycles, outperforming CCF (75.0%) and MCS (68.5%) (Figure 4h). This correlates to the smallest impedance semicircle (19.1 Ω) of CMCF compared to CCF (43.2 Ω) and MCS (53.8 Ω) obtained from electrochemical impedance spectroscopy (EIS) (Figure S13, Supporting Information). The observed fluctuations in the data points most likely stem from external environmental disturbances impacting the electrode/electrolyte interface stability and the precision of the testing instruments (Figure S14, Supporting Information). The improvement in testing precision can alleviate capacity fluctuations (Figure S15, Supporting Information).

To further elucidate the origin of the decent capacitance and rate performance, insights into the dynamic interaction energies of [EMIM]$^+$ in the bilayer and monolayer confinement pores are obtained through density functional theory (DFT) calculations. The bilayer graphene structure with slit pores is employed to approximate the slit pore model employed in determining pore size distribution. Given the larger size of [EMIM]$^+$ (0.76 nm) compared to [BF_4]$^-$ (0.45 nm) adsorbed in carbon electrodes, this study focuses on the dynamic adsorption process of [EMIM]$^+$ near both the bilayer confinement pores (1.32 nm) and monolayer confinement pores (0.78 nm). We also study the adsorption behavior within the primary pore size of 0.58 nm in CCF, which is smaller than the length but larger than the width (0.43 nm) of [EMIM]$^+$. Theoretical analyses reveal intricate dynamics regarding the interaction energy between [EMIM]$^+$ and bilayer versus monolayer confinement pores. Specifically, bilayer confinement pores demonstrate a low interaction energy with [EMIM]$^+$, which facilitates favorable charging dynamics (**Figure** 5a,b; Figure S16a and Table S2, Supporting Information).[28] Conversely, monolayer confinement pores exhibit a higher interaction energy with [EMIM]$^+$, thereby promoting efficient capacitance storage of [EMIM]$^+$ (Figure 5a,c; Figure S16b and Table S3, Supporting Information).[29] However, when it comes to pores with a diameter (0.58 nm) smaller than the length of [EMIM]$^+$, an intriguing phenomenon emerges (Figure 5a,d; Figure S16c and Table S4, Supporting Information); At the pore edge, there is a notable spike in interaction energy, suggesting the strong affinity of 0.58 nm pores for [EMIM]$^+$. Nevertheless, the interaction energy rapidly decreases as the ions penetrate further into the pore, indicating unfavorable entry processes. As a result, the combination of monolayer and bilayer confinement pores in CMCF promotes

a synergistic enhancement in energy density and charging dynamics.

To expand the application scenes, the electrochemical performances of CMCF were measured in the temperature range from 25 to 90 °C in a two-electrode setup. CV curves at 100 mV s^{-1} exhibit nearly rectangular shapes (Figure S17, Supporting Information). The observed increase in response current density with temperature can be attributed to the reduction in viscosity of [EMIM][BF_4]. GCD curves at 5 A g^{-1} display nearly symmetrical triangular shapes with prolonged charge/discharge durations, indicating enhanced capacitive performance. With the increase of temperature from 25 to 80 °C, the Nyquist plots exhibit a gradual decrease in intercepts at high frequencies, a reduction in semicircles at intermediate frequencies, and an increase in steep oblique lines at low frequencies, in accordance with the Arrhenius formula. However, a large impedance is observed at 90 °C, indicating potential instability of the electrode/electrolyte interface at this temperature. The capacitance is stable during cycling at 5 A g^{-1} for every 10 cycles across temperatures from 25 to 90 °C, demonstrating good thermal stability up to 90 °C. The incremental capacitance with temperature accords well with the CV and GCD results.

Due to the detrimental effect of trace water in [EMIM][BF_4], dehydration treatment is necessary before they are used in devices. To illustrate this, we compared the electrochemical performance of supercapacitors in [EMIM][BF_4] IL electrolytes with and without dehydration treatment.[29b] The as-purchased IL electrolyte (without dehydration) corresponds to prolonged charging times (Figure S18, Supporting Information). The lower capacitance at high currents can be attributed to the decrease in electrolyte ion density due to the presence of trace water, as evidenced by thinner CV curves at high scan rates. Because of the electrolyte decomposition, a higher capacitance is observed at low current densities, as illustrated by the appearance of polarization and redox peaks in CV curves at low scan rates. EIS curves indicate that trace water partially disrupts the Coulombic ordering of [EMIM][BF_4], consequently reducing both electrolyte and material resistances. Continuous electrolyte decomposition leads to the disrupt of the cycling continuity.

3. Conclusion

We have constructed a compressed micropore-rich carbon framework with ionophilic monolayer and bilayer confinement pores for electrochemical capacitive ion storage. The symmetric supercapacitor based on CMCF electrodes delivers a high energy density of 108.8 Wh kg^{-1} at 946.3 W kg^{-1}. The deployment of in situ Raman characterization in this study allows us to unravel the ion storage mechanism by detecting the G-band shift in confinement-pore carbons during capacitive states. We have established that the ion storage within the ionophilic confinement pores includes the following processes: voltage-induced ion gradient filling in micropores, ion exchange, and co-ion desorption, and the synergistic effect of coupled monolayer and bilayer confinement on the energy density and dynamics of the device. This study expands our comprehension on the ion behavior within confinement pores and guide the design of high-energy density supercapacitors.

Supporting Information

Supporting Information is available from the Wiley Online Library or from the author.

Acknowledgements

This work was supported by the National Natural Science Foundation of China (52072283, 52127816), the Ministry of Education, Singapore, AcRF Tier 1 (1RG80/22), and the program of China Scholarship Council (202306950008).

Conflict of Interest

The authors declare no conflict of interest.

Data Availability Statement

The data that support the findings of this study are available from the corresponding author upon reasonable request.

Keywords

confinement pore, in situ characterization, ionic liquid, porous carbon, supercapacitor

Received: March 26, 2024
Revised: July 27, 2024
Published online: August 11, 2024

[1] a) P. Simon, Y. Gogotsi, *Nat. Mater.* **2020**, *19*, 1151; b) E. Mourad, L. Coustan, P. Lannelongue, D. Zigah, A. Mehdi, A. Vioux, S. A. Freunberger, F. Favier, O. Fontaine, *Nat. Mater.* **2016**, *16*, 446; c) Z. Li, S. Gadipelli, H. Li, C. A. Howard, D. J. L. Brett, P. R. Shearing, Z. Guo, I. P. Parkin, F. Li, *Nat. Energy* **2020**, *5*, 160; d) X. Feng, X. Shi, J. Ning, D. Wang, J. Zhang, Y. Hao, Z. Wu, *eScience* **2021**, *1*, 124.

[2] a) S. Kondrat, G. Feng, F. Bresme, M. Urbakh, A. A. Kornyshev, *Chem. Rev.* **2023**, *123*, 6668; b) J. Wu, *Chem. Rev.* **2022**, *122*, 10821; c) K. Ge, H. Shao, P.-L. Taberna, P. Simon, *ACS Energy Lett.* **2023**, *8*, 2738.

[3] a) B. Jia, B. Zhang, Z. Cai, X. Yang, L. Li, L. Guo, *eScience* **2023**, *3*, 100112; b) V. Šedajová, A. Bakandritsos, P. Błoński, M. Medveď, R. Langer, D. Zaoralová, J. Ugolotti, J. Dzíbelová, P. Jakubec, V. Kupka, M. Otyepka, *Energy Environ. Sci.* **2022**, *15*, 740; c) R. Paul, Q. Zhai, A. K. Roy, L. Dai, *Interdiscip. Mater.* **2022**, *1*, 28; d) G. Li, Y. Chen, L. Yan, Q. Gong, G. Chen, L. Yang, Q. Wu, X. Wang, Z. Hu, *Small* **2022**, *18*, 2107082.

[4] a) Y.-L. Wang, B. Li, S. Sarman, F. Mocci, Z.-Y. Lu, J. Yuan, A. Laaksonen, M. D. Fayer, *Chem. Rev.* **2020**, *120*, 5798; b) K. Dong, X. Liu, H. Dong, X. Zhang, S. Zhang, *Chem. Rev.* **2017**, *117*, 6636; c) P. Simon, Y. Gogotsi, *Joule* **2022**, *6*, 28; d) S. Fleischmann, Y. Zhang, X. Wang, P. T. Cummings, J. Wu, P. Simon, Y. Gogotsi, V. Presser, V. Augustyn, *Nat. Energy* **2022**, *7*, 222.

[5] a) E. H. Lahrar, A. Belhboub, P. Simon, C. Merlet, *ACS Appl. Mater. Interfaces* **2019**, *12*, 1789; b) J. Chmiola, G. Yushin, Y. Gogotsi, C. Portet, P. Simon, P. L. Taberna, *Science* **2006**, *313*, 1760; c) X. Li, C. Cai, P. Hu, B. Zhang, P. Wu, H. Fan, Z. Chen, L. Zhou, L. Mai, H. J. Fan, *Adv. Mater.* **2024**, *36*, 2400184.

[6] a) Y. Zhu, S. Murali, M. D. Stoller, K. J. Ganesh, W. Cai, P. J. Ferreira, A. Pirkle, R. M. Wallace, K. A. Cychosz, M. Thommes, D. Su, E. A. Stach,

R. S. Ruoff, *Science* **2011**, *332*, 1537; b) N. Yang, S. Yu, W. Zhang, H. M. Cheng, P. Simon, X. Jiang, *Adv. Mater.* **2022**, *34*, 2202380; c) Y. Li, H. Shao, Z. Lin, J. Lu, L. Liu, B. Duployer, P. O. Å. Persson, P. Eklund, L. Hultman, M. Li, K. Chen, X.-H. Zha, S. Du, P. Rozier, Z. Chai, E. Raymundo-Piñero, P.-L. Taberna, P. Simon, Q. Huang, *Nat. Mater.* **2020**, *19*, 894.

[7] a) K. Breitsprecher, M. Janssen, P. Srimuk, B. L. Mehdi, V. Presser, C. Holm, S. Kondrat, *Nat. Commun.* **2020**, *11*, 6085; b) L. Sun, K. Zhuo, Y. Chen, Q. Du, S. Zhang, J. Wang, *Adv. Funct. Mater.* **2022**, *32*, 2203611.

[8] a) R. Futamura, T. Iiyama, Y. Takasaki, Y. Gogotsi, M. J. Biggs, M. Salanne, J. Ségalini, P. Simon, K. Kaneko, *Nat. Mater.* **2017**, *16*, 1225; b) M. Antonietti, X. Chen, R. Yan, M. Oschatz, *Energy Environ. Sci.* **2018**, *11*, 3069.

[9] S. Kondrat, A. Kornyshev, *J. Phys. Condens. Matter.* **2013**, *25*, 119501.

[10] a) H. Shao, Y.-C. Wu, Z. Lin, P.-L. Taberna, P. Simon, *Chem. Soc. Rev.* **2020**, *49*, 3005; b) C. Lian, D. Jiang, H. Liu, J. Wu, *J. Phys. Chem. C* **2016**, *120*, 8704.

[11] a) J. Ye, Y.-C. Wu, K. Xu, K. Ni, N. Shu, P.-L. Taberna, Y. Zhu, P. Simon, *J. Am. Chem. Soc.* **2019**, *141*, 16559; b) J. Tan, Z. Li, M. Ye, J. Shen, *ACS Appl. Mater. Interfaces* **2022**, *14*, 37259.

[12] X. Li, Z. Liu, C. Cai, Q. Yu, W. Jin, M. Xu, C. Yu, S. Li, L. Zhou, L. Mai, *ChemSusChem* **2021**, *14*, 1756.

[13] J. Sun, R. Wang, H. Li, L. Zhang, S. Liu, *Mater. Today Energy* **2023**, *33*, 101273.

[14] E. M. Alhajji, J. Yin, J. Jin, M. N. Hedhili, U. Schwingenschlögl, H. N. Alshareef, *Mater. Today Energy* **2023**, *38*, 101404.

[15] P. Zhang, L. Wang, S. Yang, J. A. Schott, X. Liu, S. M. Mahurin, C. Huang, Y. Zhang, P. F. Fulvio, M. F. Chisholm, S. Dai, *Nat. Commun.* **2017**, *8*, 15020.

[16] a) E. Zhang, Y.-C. Wu, H. Shao, V. Klimavicius, H. Zhang, P.-L. Taberna, J. Grothe, G. Buntkowsky, F. Xu, P. Simon, S. Kaskel, *J. Am. Chem. Soc.* **2022**, *144*, 14217; b) J. M. Griffin, A. C. Forse, W.-Y. Tsai, P.-L. Taberna, P. Simon, C. P. Grey, *Nat. Mater.* **2015**, *14*, 812; c) Y. Wang, C. Malveau, D. Rochefort, *Energy Storage Mater.* **2019**, *20*, 80.

[17] X. Wang, J. Liu, Z. Liu, W. Wang, J. Luo, X. Han, X. Du, S. Qiao, J. Yang, *Adv. Mater.* **2018**, *30*, 1800005.

[18] a) M. A. Reddy, H. M. Joseph, A. Gross, M. Fichtner, H. Euchner, *ACS Energy Lett.* **2018**, *3*, 2851; b) L. J. Hardwick, P. W. Ruch, M. Hahn, W. Scheifele, R. Kötz, P. Novák, *J. Phys. Chem. Solids* **2008**, *69*, 1232; c) M. Inaba, H. Yoshida, Z. Ogumi, *J. Electrochem. Soc.* **1996**, *143*, 2572.

[19] E.-S. Jang, C.-W. Kang, *Wood Sci. Technol.* **2022**, *56*, 883.

[20] a) F. Chen, T. You, Y. Yuan, C. Pei, X. Ren, Y. Huang, Z. Yu, X. Li, H. Zheng, Y. Pan, K. Yang, L. Wang, *J. Chem. Phys.* **2017**, *146*, 094502; b) N. E. Heimer, R. E. Del Sesto, Z. Meng, J. S. Wilkes, W. R. Carper, *J. Mol. Liq.* **2006**, *124*, 84; c) M. A. Harris, T. Kinsey, D. V. Wagle, G. A. Baker, J. Sangoro, *Proc. Natl. Acad. Sci* **2021**, *118*, 2020878118.

[21] a) F. W. Richey, B. Dyatkin, Y. Gogotsi, Y. A. Elabd, *J. Am. Chem. Soc.* **2013**, *135*, 12818; b) F. W. Richey, C. Tran, V. Kalra, Y. A. Elabd, *J. Phys. Chem. C* **2014**, *118*, 21846; c) T. Romann, O. Oll, P. Pikma, H. Tamme, E. Lust, *Electrochim. Acta* **2014**, *125*, 183.

[22] A. C. Forse, C. Merlet, J. M. Griffin, C. P. Grey, *J. Am. Chem. Soc.* **2016**, *138*, 5731.

[23] a) C. Merlet, B. Rotenberg, P. A. Madden, P.-L. Taberna, P. Simon, Y. Gogotsi, M. Salanne, *Nat. Mater.* **2012**, *11*, 306; b) J. Li, P. J. Burke, *Nat. Commun.* **2019**, *10*, 3598.

[24] C. Lian, X. Kong, H. Liu, J. Wu, *J. Phys. Condens. Matter* **2016**, *28*, 464008.

[25] Z. Lian, H. Chao, Z.-G. Wang, *ACS Nano* **2021**, *15*, 11724.

[26] a) K. Breitsprecher, C. Holm, S. Kondrat, *ACS Nano* **2018**, *12*, 9733; b) C. Lian, A. Gallegos, H. Liu, J. Wu, *Phys. Chem. Chem. Phys.* **2017**, *19*, 450.

[27] a) X. Yang, C. Cheng, Y. Wang, L. Qiu, D. Li, *Science* **2013**, *341*, 534; b) J. Li, N. Wang, J. Tian, W. Qian, W. Chu, *Adv. Funct. Mater.* **2018**, *28*, 1806153; c) Z. Song, H. Duan, L. Miao, L. Ruhlmann, Y. Lv, W. Xiong, D. Zhu, L. Li, L. Gan, M. Liu, *Carbon* **2020**, *168*, 499; d) J. Liu, L. Ma, Y. Zhao, H. Pan, H. Tang, H. Zhang, *Chem. Eng. J.* **2021**, *411*, 128573; e) Z. Song, H. Duan, L. Li, D. Zhu, T. Cao, Y. Lv, W. Xiong, Z. Wang, M. Liu, L. Gan, *Chem. Eng. J.* **2019**, *372*, 1216; f) Q. Du, Y. Zhao, K. Zhou, Y. Chen, L. Yang, C. Wang, J. Wang, *Nanoscale* **2021**, *13*, 13285.

[28] a) T. Mo, J. Peng, W. Dai, M. Chen, V. Presser, G. Feng, *ACS Nano* **2023**, *17*, 14974; b) S. Kondrat, P. Wu, R. Qiao, A. A. Kornyshev, *Nat. Mater.* **2014**, *13*, 387.

[29] a) X. Wang, M. Salari, D. Jiang, J. C. Varela, B. Anasori, D. J. Wesolowski, S. Dai, M. W. Grinstaff, Y. Gogotsi, *Nat. Rev. Mater.* **2020**, *5*, 787; b) P. Simon, Y. Gogotsi, *Nat. Mater.* **2021**, *20*, 1597.